Applied Magnetic Resonance
https://doi.org/10.1007/s00723-024-01702-7

Applied
Magnetic Resonance

ORIGINAL PAPER

Towards an EPR on a Chip Spectrometer for Monitoring Radiation Damage During X-ray Absorption Spectroscopy

Ekaterina Shabratova · Hadi Lotfi · Ayman Sakr · Mohamed Atef Hassan · Michal Kern · Matthias Neeb, René Grüneberger[4] · Bastian Klemke[4] · Gianluca Marcozzi[1,3] · Klaus Kiefer[4] · Aleksei Tsarapkin[5] · Katja Höflich[5] · Alina Dittwald[6] · Andrea Denker[6] · Jens Anders[2] · Joseph E. McPeak[1,7] · Klaus Lips[1,3]

Received: 5 June 2024 / Revised: 31 July 2024 / Accepted: 12 August 2024

Abstract

Electron paramagnetic resonance (EPR) spectroscopy is an essential tool to investigate the effects of ionizing radiation, which is routinely administered for reducing contaminations and waste in food products and cosmetics as well as for sterilization in industry and medicine. In materials research, EPR methods are not only employed as a spectroscopic method of structural investigations, but also have been employed for detection of changes in electronic structure due to radiation damage from high energy X-rays, for example, to monitor radical formation inside biomolecules caused by X-ray irradiation at carbon, nitrogen, and oxygen K-edges at synchrotron facilities. Here a compact EPR spectrometer, based on EPR-on-a-chip (EPRoC) sensor and a portable electromagnet, has been developed as a solution for monitoring radiation damage of samples during their investigation by X-ray absorption spectroscopy (XAS) at synchrotron facilities. A portable electromagnet with a soft iron core and forced air temperature stabilization was constructed as the source of the external magnetic field. The sweep range of magnetic field inside the most homogeneous region of the portable electromagnet is 12–290 mT. The compact spectrometer performance was evaluated by placing the EPRoC sensor inside either a commercial electromagnet or the portable electromagnet to record the EPR spectrum of tempol, irradiated alanine, and dilithium phthalocyanine (Li_2Pc). The potential performance of the portable spectrometer for the detection of radiation damage in organic compounds and transition metal-containing catalysts during XAS measurements in both fluorescence and transmission modes was calculated with promising implications for measurements after implementation in a synchrotron-based XAS spectrometer.

Extended author information available on the last page of the article

Published online: 03 September 2024

1 Introduction

Electron paramagnetic resonance (EPR) is an important tool to detect and investigate the electronic properties of paramagnetic materials. It is highly effective in detecting and studying radicals and EPR-active transition metals that are present in many biological systems. One important application of EPR is monitoring the radiation dose of food products, cosmetics, and drugs after their sterilization via ionizing radiation of gamma- and X-rays or electron beams [1–4]. It was found that gamma rays generate paramagnetic centers inside the bone fragments contained within meat products which has led the European Committee for Standardization to adopt EPR as one of the methods employed to identify irradiated food [5]. EPR has also been applied to detect radicals generated in antibiotics like piperacillin, ampicillin, and crystalline penicillin after their sterilization with gamma-irradiation which may potentially reduce the pharmacological activity and alter the pharmacokinetic properties of the drugs. It has been shown that gamma radiation can induce formation of up to 10^{17} spins/g in penicillin [6]. For comparison, a tiny fragment (10^{-8} g) of 2,2-diphenyl-1-picrylhydrazyl (DPPH) contains about 10^{14} spins and is commonly used as a standard sample for quantitative EPR measurements due to its strong EPR signal [7].

In industrial and medical fields, EPR can be used to measure the radiation dose absorbed by alanine in reference dosimeters [8–11]. Alanine dosimetry has been evaluated in clinical trials for the precision with which the radiation dose received by a patient during radiotherapy may be determined. It was demonstrated that precisions between 1 and 6% could be achieved for various irradiation methods [12]. Several studies have shown that EPR-sensitive tooth dosimetry can be successfully applied to assess the exposure of patients to ionizing radiation after a high-radiation exposure event [13, 14]. In addition to dosimetry measurements, EPR is commonly utilized in chemistry and biology together with X-ray absorption spectroscopy (XAS) to investigate important structural parameters like symmetry, bonding and ligand properties of complex molecules such as blue copper and iron-sulfur proteins [15–17].

While EPR is a non-destructive method, X-ray irradiation often damages the samples under interrogation [18–21]. It has been demonstrated that after only 10 min of X-ray absorption near edge structure (XANES) measurements at the Cu K-edge (~9000 eV) on Cu(II) organometallic species (Cu^{II}(TMEDA)@Al_2O_3, where (TMEDA) = tetramethylethylenediamine), the concentration of Cu(I) species in the sample can increase by a factor of 2 after the reduction of Cu(II) species due to ionizing radiation [22]. As Cu(II) is paramagnetic while Cu(I) and Cu(0) are diamagnetic, the radiation damage in Cu(II) will be detected in EPR as a decrease of the signal intensity during the XANES measurement. A similar approach has been demonstrated in biomolecules irradiated by soft X-ray radiation at the SPring-8 synchrotron facility [23]. A cavity of an X-band EPR spectrometer was integrated into a high-vacuum chamber connected to the beamline. The spectrometer was found to successfully determine the radical formation induced by ionizing radiation. While

EPR can be a useful tool for assessing damage caused by the ionizing radiation present during X-ray spectroscopy experiments, it is not commonly implemented in XAS spectrometers likely due to high costs and technological complexity of modern EPR devices. A critically coupled, high quality factor (Q) resonator is typically used in conventional EPR spectrometers that creates a significant spatial limitation for sample access, especially when considering implementing EPR detection into an existing technology. Similarly, big electromagnets are typically used such that a conventional EPR spectrometer cannot easily be integrated inside the measurement chamber of an X-ray spectrometer.

Spatial restrictions aside, the detection system for XAS must be considered. The XAS signal can be recorded in three modes: transmission, fluorescence, and electron yield; the last of which will be omitted because the influence of the applied magnetic field, required for EPR experiments, disrupts the trajectories of the emitted Auger electrons. In transmission geometry, the intensity of the incident X-ray beam is measured together with the intensity of the beam after it has passed through the sample. It is, therefore, the ratio between these intensities that determines the absorption spectrum. In fluorescence mode, the detector is placed perpendicular to the direction of the incident X-ray beam. Atoms inside the sample absorb the X-ray radiation, forming excited states while leaving vacancies in one of their core orbitals. If the empty core level becomes occupied by an electron from a higher energy level, X-rays of lower energy will be emitted in random directions to be detected by the fluorescence detector [24]. While transmission mode is recommended for measurements of concentrated and homogeneous materials, diluted and non-homogeneous samples are commonly measured via fluorescence detection [25]. The integration of EPR into an XAS spectrometer will, therefore, require a highly tailored design, such as that of a small, resonator-free EPR spectrometer to provide access to EPR measurements in existing X-ray chambers.

It has been recently demonstrated that utilizing EPR-on-a-chip (EPRoC) technology alleviates the spatial restrictions of the conventional spectrometer to allow EPR measurements in a confined environment [26–28]. The EPRoC contains a voltage-controlled oscillator (VCO), which functions both as the microwave source by producing microwaves and as the detector via inductively detecting the EPR signal as a change in either the amplitude or the frequency of the oscillation. To this end, we herein present such a portable spectrometer where the microwave source and detection system are comprised of a single-coil VCO while the external B_0 field is swept via a portable electromagnet (EM). The EPRoC-based spectrometer is small enough to be integrated into XAS spectrometers and monitor radiation damage caused during X-ray investigations. The scheme of a potential synchrotron-based deployment of the X-ray compatible EPRoC spectrometer is presented in Fig. 1. To further tailor the EPRoC spectrometer to the synchrotron environment, an EPRoC with a hole through the silicon chip containing the VCO was fabricated via focused ion beam (FIB) milling to enable the additional possibility for both fluorescence and transmission modes of XAS measurements in the event that both detection schemes are available in the host chamber.

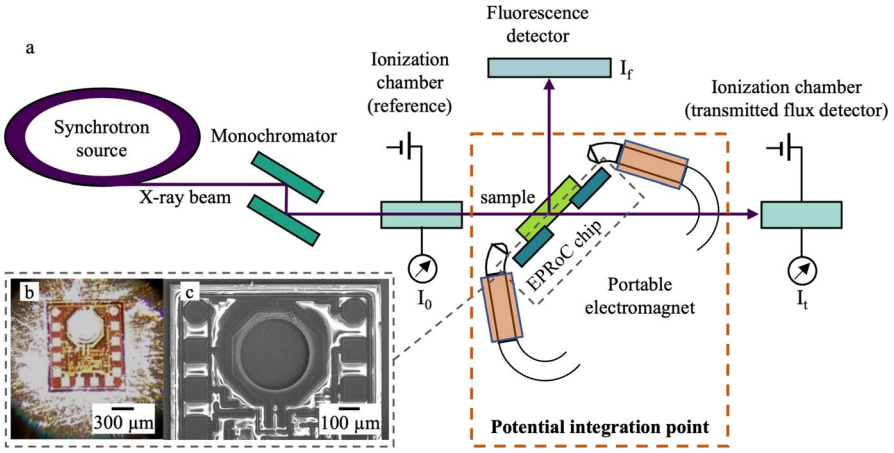

Fig. 1 **a** Scheme of the possible integration of the portable EPRoC-based spectrometer into a typical XAS measurement chamber for radiation damage detection during synchrotron XAS experiment in fluorescence mode (with fluorescence detector) and transmission mode (with transmitted flux detector). **b** Photo of the EPRoC with a hole drilled inside coil. **c** Scanning electron microscopy image of the hole inside the EPRoC

2 Methods

2.1 Sample Preparation

To estimate EPRoC spin sensitivity mixed powder samples of known spin concentrations were prepared from 4-hydroxy-2,2,6,6-tetramethylpiperidinyloxyl (tempol) and sucrose octa-acetate (SuO) in proportions ranging from 1 to 100% w/w. The number of spins (N_S) inside the sensitive volume of the EPRoC was estimated to be between 10^{14} and 10^{16} total spins assuming an ellipsoidal cylinder with a volume of 7.2 nL as the active area of the EPRoC coil, approximated after appropriate scaling from the determination of the sensitive volume and B_1 distribution in a smaller VCO coil [29].

Alanine powder (MP Biomedicals) was placed inside glass vials and irradiated using a cobalt source for exposure to gamma-radiation. The dose rate was measured inside a Farmer chamber with a calibrated Unidos, used to readout values of the current. The sample was exposed to constant irradiation at the maximum achievable rate for 9 days before being removed from the irradiation chamber. The estimated total radiation dose of the sample was around 16 kGy. The spin concentration of the sample was measured by conventional EPR spectroscopy by comparison of the double integral intensity of a Bruker irradiated alanine standard. The number of spins per cubic millimeter was then calculated for comparison with the active volume of the single-coil EPRoC and resulted in a total number of spins inside the sensitive volume of the EPRoC of $9.6 \cdot 10^{12}$.

Samples were placed directly onto the EPRoC in an excess amount to completely cover the entire area of the VCO. This ensured that the sensitive volume of EPRoC would be completely filled with the sample reducing sample placement errors when comparing total signal intensity between samples. All samples were measured in powder form and under normal atmosphere. After each measurement, the EPRoC surface was gently cleaned with ethanol.

2.2 Portable Electromagnet

For establishing the external B_0 field, a small electromagnet (25 × 20 cm) was designed such that the magnetic field can be swept between 12 and 290 mT. Due to the fact that the EPRoC should work both in transmission and reflection XAS mode and due to limited space inside the vacuum chamber of the X-ray instrumentation, permanent magnets that have sufficient field strength for C-band (here 7 GHz) with the necessary homogeneity criteria are not easily constructed. The core of the electromagnet was constructed from soft iron (Vimvar, Type 1, ASTM A848-01) and the tips were machined from an iron-cobalt-vanadium alloy (Hiperco 50, Type 1, UNS R 30005, ASTM A801) supplied by Nicofe Materials Ltd. For the coil construction, enameled copper wire with a diameter of 1 mm was used. The magnet is equipped with a forced-air cooling system to increase thermal stability and prevent overheating. The intended installation would isolate the majority of the magnet, including the necessary air cooling, outside of the UHV chambers such that only the pole shoes would be integrated into the measurement cell. In this case, the sample space can be separated from the vacuum chamber by a silicon nitride window. Using a current of 1.87 A supplied to the coils via a programmable benchtop power supply (RND 320-KA3305P) a magnetic field of 250 ± 0.1 mT in the most homogeneous region was generated, which corresponded to the resonance position of the EPRoC for most organic radicals ($g = 2$). The magnetic field was measured for different positions of the Hall probe placed close to the central point between the pole shoes. The position was varied in steps of 0.1 mm. The position of the Hall probe where the magnetic field was at a maximum within the y- and z-directions while at a minimum in the x-direction was determined to be the most homogeneous region. The center of the region corresponded to the center of the pole shoes with coordinates $x = 0$, $y = 0$, $z = 0$. The mapping of the magnetic field within the xy-plane was performed around the center of the pole shoes by recording the magnetic field at varying positions of the Hall probe. The error in measuring the absolute magnetic field was determined by the precision of the gaussmeter and probe (LakeShore 421). A graphical depiction of the portable EM and the field mapping around the region where the magnetic field is most homogeneous is given in Fig. 2. The homogeneous region was found to be quite small (1–2 mm) such that outside of this region the magnetic field increases dramatically (3–9 mT); however, the area of high homogeneity was sufficiently large to encompass the width of the VCO coil of the EPRoC.

To accurately control the B_0 field while sweeping through resonance, two Hall probes were used to properly calibrate the system before performing EPR measurements (Fig. S1). The magnetic field was first measured inside

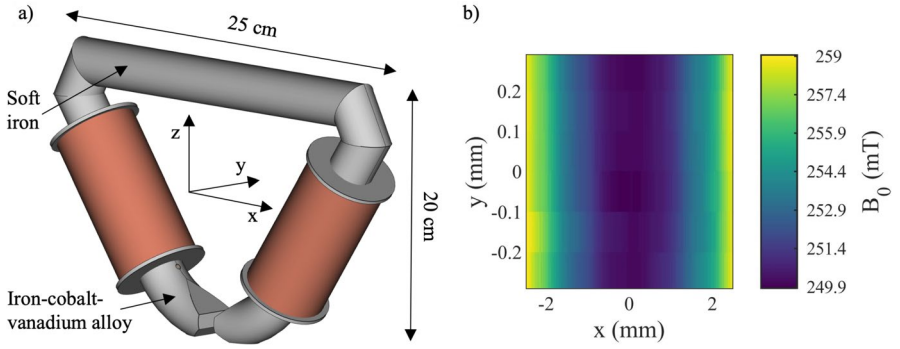

Fig. 2 **a** 3D graphical depiction of the portable electromagnet. The current supplied to the coils (1.87 A) resulted in a magnetic field of 250 ± 0.1 mT. **b** A map of the magnetic field measured in the middle of the pole shoe of the portable electromagnet where the magnetic field is the most homogeneous, centered at $x=0$, $y=0$ in the plot

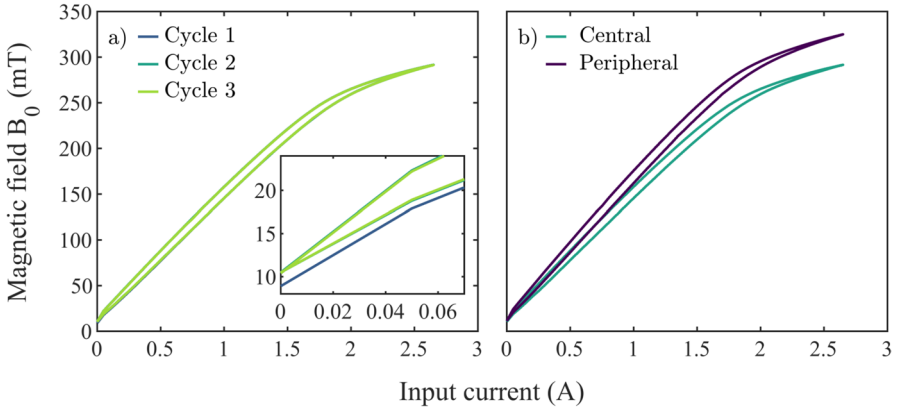

Fig. 3 **a** The hysteresis curves of the portable EM during subsequent current cycles. Only negligible changes were observed between the second and third current cycles demonstrating that thermal equilibrium was achieved. **b** The hysteresis curves of magnetic field when recorded using the Hall probe placed inside the most homogeneous region of the magnet (central probe) and the Hall probe placed on the adjacent side closest to the pole shoe of the magnet (peripheral probe)

the most homogeneous region using a single Hall probe placed in the center of the poles (central probe) while repeatedly cycling the current (0–2.65 A) supplied to the coils with a step size of 0.05 A. Magnetic field values were recorded using a gaussmeter (LakeShore 421). A change in the magnetic field response with respect to the supplied current was observed between the first and second recorded cycles; however, only negligible changes were observed in subsequent cycles demonstrating that thermal equilibrium was achieved (Fig. 3a). An additional Hall probe, connected to a separate teslameter (Projekt Elektronik FM 302) was placed peripherally to the central probe, on the right side of one of the

pole shoes of the portable EM (peripheral probe). During calibration, the current inside the coils was swept between 0 and 2.65 A while the magnetic field was recorded from both probes. Figure 3b depicts the dependence of the field detected by the central probe (B_i^{central}, in blue) and the field detected by the peripheral probe ($B_i^{\text{peripheral}}$, in purple) on the current across the coils of the magnet. To accurately determine the intensity of the magnetic field in the center of the magnet from the magnetic field recorded by the peripheral probe, the B_i^{central} values were approximated as a comparative 10th order polynomial function, p, with respect to the $B_i^{\text{peripheral}}$ values, minimizing the function,

$$\sum_{i=0}^{N} \left| p\left(B_i^{\text{peripheral}}\right) - B_i^{\text{central}} \right|^2$$

where N is the number of data points recorded during the measurement. The polynomial function p was then used to calculate values of the magnetic field within the most homogeneous region of the magnet ($B_i^{\text{calculated}}$) from those recorded using the peripheral probe for every value of the current as follows,

$$B_i^{\text{calculated}} = p\left(B_i^{\text{peripheral}}\right), \sigma = \sqrt{\frac{1}{N}\sum_{i=0}^{N} \left| B_i^{\text{calculated}} - B_i^{\text{central}} \right|^2}$$

The error, σ, attributed to the values of the magnetic field was estimated as the root mean square deviation between the calculated magnetic field and the actual measured values, as shown in the above equation, resulting in $\sigma = 0.101 \pm 0.003$ mT. The value of σ obtained is comparable to the sensitivity of the teslameter and gaussmeter used for the magnetic field measurements and may be considered as the overall error for the calculated magnetic field values within the most homogeneous region. Upon conclusion of the calibration procedure, the central probe was removed and the EPRoC was placed in the center of portable electromagnet. During the EPR measurements the field was swept by changing the current inside the coils while the values of the peripheral probe were recorded to calculate the B_0 field present at the location of the EPRoC in the magnetic field. A settling time of 4 s was chosen to ensure that the electromagnet has reached thermal equilibrium before measuring at each field position in the recorded spectrum. The calibration procedure as well as all EPRoC measurements inside the portable electromagnet were controlled using home-written Python scripts executed within the open-source software package Qudi [30].

2.3 EPR-on-a-Chip (EPRoC)

A chip-integrated voltage-controlled-oscillator-based EPR spectrometer was used as both the microwave source and the detector. The chip consists of a LC-tank VCO and a phase-locked loop (PLL) that stabilizes the VCO frequency. The detection principle is similar to previously published works [26] however, the chip reported herein was manufactured in the 130 nm IHP SG13S bipolar complementary

metal–oxide–semiconductor (BiCMOS) technology. In short, the VCO consists of a single octagonal coil with a diameter of 400 µm, a voltage-controlled capacitor (varactor), and a cross-coupled transistor pair to compensate for the energy lost in the resulting LC oscillator similar to previous EPRoC designs [28, 31, 32]. The VCO was designed to generate microwave fields (B_1) in the C-band with frequencies ranging from 6.656 to 7.056 GHz. To ensure a stable B_1-field frequency against process-voltage-temperature (PVT) variations, the VCO is embedded in an integer-N PLL with a feedback frequency divisor of $N=4$. Reference frequencies between 1.664 and 1.764 GHz were supplied at the PLL input by a Rohde and Schwarz SMIQ 04B RF signal generator. Frequency modulation (FM) of the reference frequency is applied instead of the field modulation used in conventional EPR, thus eliminating the necessity for additional field-modulation coils. Because of the closed-loop operation of the EPRoC sensor, EPR-induced frequency perturbations in the VCO are corrected within the PLL bandwidth, enabling implicit demodulation and direct measurement at the varactor control terminal. The EPR signal is recorded via a change in the LC tank oscillation frequency, rather than the typical MW absorption measurement employed in conventional EPR, and a dispersion-like signal is obtained [29, 33–35]. EPR measurements were performed by inserting the EPRoC, placed on a printed circuit board, between the poles of either a commercial electromagnet (Bruker B-E 25 electromagnet and ER 083 power supply, large EM) from a Bruker ESP300 spectrometer or a portable electromagnet (portable EM, see Sect. 2.4). The EPR signal was recorded by keeping the oscillation frequency of the EPRoC constant while sweeping the magnetic field, B_0, and was acquired using a lock-in amplifier (Anfatec eLockIn 203). A modulation frequency of 100 kHz and frequency deviation of between 500 and 800 kHz was applied to the reference frequency directly using the signal generator. Due to the PLL feedback factor of 1/4, the actual frequency deviation of the VCO frequency is between 2 and 3.2 MHz. Photos detailing the experimental configurations can be found in the Supporting information (Fig. S1).

All spectra recorded with the EPRoC were baseline corrected using a polynomial function of varying order due to the presence of a relatively intense baseline that changed independently of the magnetic field and temperature (Figure S2). The recorded spectra were simulated using the EasySpin software package available in Matlab (Mathworks) [36].

2.4 Fabrication of a Hole Inside the EPRoC

The fabrication of a hole through the VCO of the EPRoC was performed as a proof-of-concept experiment using a process similar to that reported in Ref. [37] by focused ion beam milling. Focused ion beams locally remove material based on physical sputtering providing mask-free and high-resolution patterning. The measurements presented in the current work were performed using the EPRoC before hole drilling with the sample placed directly on the surface of the VCO. The hole drilling was performed with a 30 kV gallium ion beam in a Zeiss

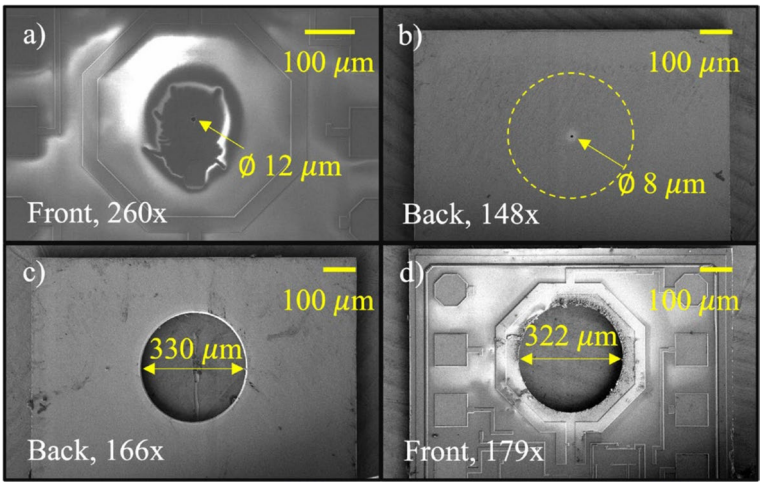

Fig. 4 Secondary electron micrographs of the hole fabrication process inside the EPRoC. **a** Image of the reference hole viewed from the front side of the EPRoC with image artefacts due to charging. **b** Image of the reference hole viewed from the back side of the EPRoC. A circular pattern for the big hole is depicted with a dashed yellow line. **c** Image of the FIB milled hole on the back side of EPRoC, and **d** the image of the resulting hole from the front side of the EPRoC

Crossbeam 340 microscope. For this purpose, the ion beam was scanned on a circular area with a circular-shaped beam path. An overview of the hole fabrication protocol is presented in Fig. 4, where the label "front" has been placed in reference to the side of the EPRoC where the VCO is closest to the surface while "back" refers to the opposite side. Since the typical spot size of the X-ray beam during synchrotron-based XAS experiments can be estimated as 200 µm × 200 µm [38], the diameter of the hole inside the VCO was chosen to be between 300 and 350 µm to allow the X-ray beam to pass through the EPRoC during XAS experiments. The diameter of holes that can be produced is limited by size of the coil, which is 400 µm. Moreover, the tailing of the ion beam, caused by increasing transverse thermal velocity, may damage the coil during the FIB milling [39]. Therefore, the milling of the hole was performed from the back of the EPRoC PCB to ensure that the ion beam tails would not damage the beam-sensitive VCO. For proper alignment of the circular pattern of the hole when viewed from the back of the PCB, a reference hole was first milled in the center of coil from the front side (Fig. 4a) using a small beam current of 30 nA, a pixel distance of 22.5 nm and an overall ion dose of 850,000 mC/cm^2. The reference hole was clearly visible from the back side (Fig. 4b) and acted as a marker for the position of the center of the coil (Fig. 4b, *yellow dashed line*). Using a large beam current of 50 nA, a pixel distance of 22.5 nm and an ion dose of 72,000 mC/cm^2, a hole with a diameter of around 330 µm was then milled from the back side of the EPRoC (Fig. 4c). The resulting hole diameter on the front side of the EPRoC is slightly reduced to around 322 µm, partly due to the non-ideal beam profile for

this very high ion current and partly due to redeposition at the side walls. The optimized FIB protocol allowed for the fabrication of the target hole diameter inside the EPRoC without damaging the coil. The preservation of EPRoC performance after FIB milling was verified and presented in [37]. After consideration of the effort required, the EPRoC devices which underwent hole-fabrication in the VCO coil were not used within the current investigation and are instead reserved for eventual installation in an XAS spectrometer.

3 Results

3.1 Evaluation of the EPRoC Inside a Commercial Electromagnet

To test the achievable sensitivity, the EPRoC was placed inside a commercial electromagnet as the B_0 homogeneity of the conventional system is well below the linewidths of the samples investigated. Further analysis of the recorded spectra was performed under the assumption that the commercial electromagnet did not play a role in any signal or baseline distortions. Tempol samples of varying spin concentrations were used to estimate the spin sensitivity of the EPRoC, the results of which are shown in Fig. 5a after the appropriate scaling factors were applied to allow visual comparison between the recorded spectra. The total number of spins is presented in a logarithmic scale and the amplitude of the FM signal (dispersion-like), the amplitude of the imaginary component of the Hilbert-transformed FM signal (absorption-like), and the twice integrated absorption-like signal or double

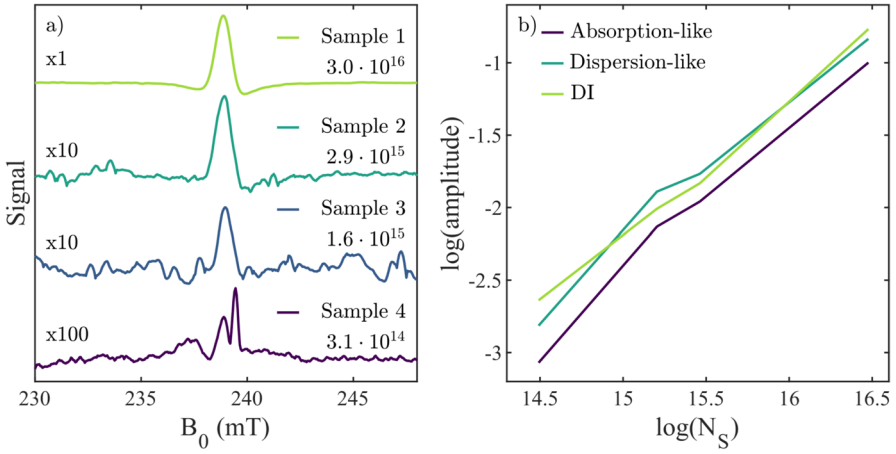

Fig. 5 **a** EPRoC spectra of tempol samples with differing total number of spins contained within the VCO coil. The spectra have been increased in scale by the factor listed above each spectrum to allow for a convenient visual comparison. **b** Dependence of the signal intensity on the total number of spins, displayed using a logarithmic-logarithmic (log–log) scale. The amplitude of the FM signal (dispersion-like), the imaginary component of the Hilbert-transformed FM signal (absorption-like), and the integrated absorption-like signal or double integral signal (DI) increase linearly with the total number of spins present inside the VCO coil

Table 1 The sample number, total number of spins present within the VCO coil of the EPRoC, the SNR with respect to the square-root of the number of acquired spectra, and the normalized amplitudes, shown as a percentage relative to the intensity observed when measuring Sample 1, of the FM-signal (dispersion-like) the Hilbert transformed FM-signal (absorption-like) and the second integral intensity of the absorption-like signal

Sample	Number of spins	SNR/$\sqrt{\text{scans}}$	Dispersion-like signal	Absorption-like signal	
			Normalized amplitude, %	Normalized amplitude, %	Normalized double integral, %
Sample 1–100%	$3.0 \cdot 10^{16}$	124	100	100	100
Sample 2–10%	$2.9 \cdot 10^{15}$	21	12	11	9
Sample 3–5%	$1.6 \cdot 10^{15}$	10	9	7	6
Sample 4–1%	$3.1 \cdot 10^{14}$	1	1	1	1

integral (denoted as DI) are shown for comparison. To increase the signal-to-noise ratio (SNR) of the recorded spectra, the FM signal was digitally filtered using a Savitzky–Golay filter with a window length of 0.5 mT. These values were chosen as to not introduce broadening of the EPR lineshape while maximizing SNR. The resulting SNR normalized to the square root of the number of acquired spectra in each measurement (SNR/$\sqrt{\text{scans}}$) is presented in the Table 1. The relative amplitudes for each dispersion-like and absorption-like signal are given as a percentage of the amplitude obtained when the entire volume of the sample is spin-containing, such that for Sample i: $p = \frac{v(\text{Sample } i)}{v(\text{Sample 1})} \cdot 100\%$, where p is the relative percent presented, v is the amplitude of dispersion-like, absorption-like, or double integral signal, and i is the number of sample ($i = 1, 2, 3, 4$).

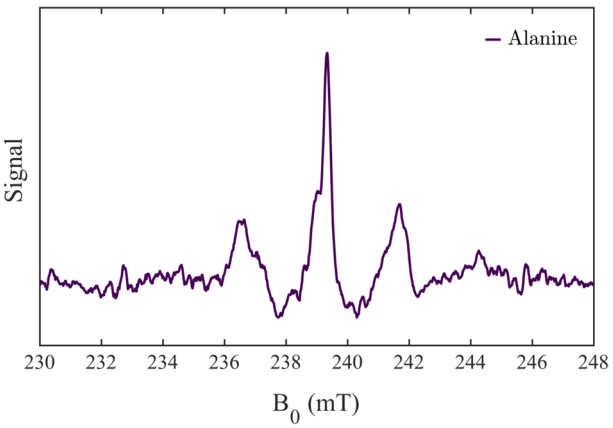

Fig. 6 EPR spectrum of irradiated alanine (9.6×10^{12} spins) after 49 acquisitions, recorded over 18 h of continuous measurement using the commercial electromagnet. From the SNR achieved (21.3), the per hour sensitivity of the EPRoC was estimated ($5.8 \cdot 10^{12}$ spins) assuming SNR = 3

To further evaluate the sensitivity of the EPRoC, an irradiated alanine sample commonly used for industrial and medical dosimetry applications [8–12] was investigated using the EPRoC and the commercial electromagnet. The EPR spectrum of alanine was recorded by averaging 49 acquired spectra which required 18 h of continuous measurement (Fig. 6). The recorded FM-signal was digitally filtered using a Savitzky–Golay filter with a window length of 0.3 mT to increase the SNR of the spectrum without broadening the linewidth of the signal. Because the SNR increases with the square root of the number of acquired spectra, it was calculated from the total SNR of the spectrum after filtering (21.3) that after only one hour of measurement time, ~ 3 acquired spectra would be recorded yielding an $\mathrm{SNR} = \frac{21.3 \cdot \sqrt{2.7}}{\sqrt{49}} = 5$. For a signal with SNR = 3 to be recorded in 1 h of measurement time, the number of spins in the sample must be equal or greater than $9.6 \cdot 10^{12} \cdot \frac{3}{5} = 5.76 \cdot 10^{12}$ total spins assuming a linear dependence of signal amplitude on the absolute number of spins inside the coil as shown in Table 1. In the absence of magnet settling time (approximately 1 s for the commercial electromagnet), the spin sensitivity observed is similar to that of similar architecture BiCMOS EPRoC devices as reported in Ref. [28]. Further information regarding sensitivity may be found in the Supporting information.

3.2 Evaluation of the EPRoC Inside the Portable Electromagnet

The capabilities of the portable electromagnet were investigated by recording the EPR spectrum of dilithium phthalocyanine (Li_2Pc) with the EPRoC and both the commercial electromagnet and the portable electromagnet. The sample was measured under normal atmosphere. The number of spins inside the sensitive volume of the EPRoC was estimated as the number of Li_2Pc particles, calculated using the measured density of the powder without consideration of particle packing, and is

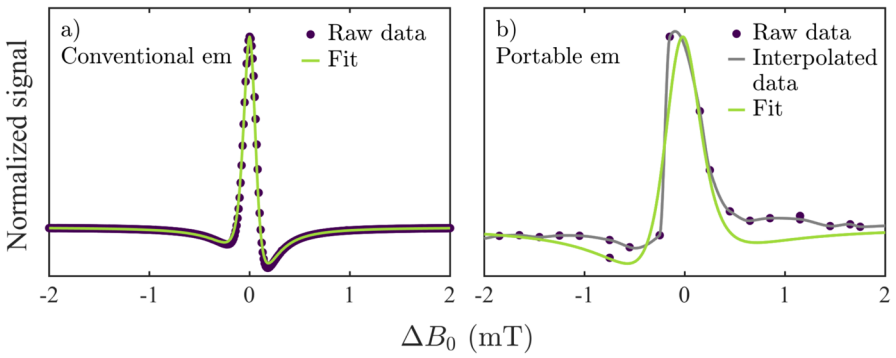

Fig. 7 **a** EPR spectrum of Li_2Pc obtained when the EPRoC is placed in the commercial electromagnet. The fit to the data obtained via simulation and least-squares analysis is shown in green. **b** EPR spectrum of Li_2Pc obtained when the EPRoC is placed in the portable electromagnet. The data were interpolated (*grey*) before performing a fit to the data (*green*) as performed in (**a**). Spectra are presented as the change in magnetic field with respect to the observed resonance position, see text

approximately $3.7 \cdot 10^{15}$. The spectrum was first obtained using the commercial electromagnet, from which the resonance position and lineshape of Li_2Pc when recorded using the EPRoC were obtained (Fig. 7a). The spectrum was subsequently recorded for comparison with the EPRoC placed between the poles of the portable electromagnet after the calibration routine was completed, replacing the central probe within the homogeneous region of the magnetic field (Fig. 7b). Both spectra are presented as the dependence of the EPRoC signal from the deviation of the measured magnetic field from the resonance position $\Delta B_0 = B_0 - B_{0,\mathrm{res}}$, where B_0 is the magnetic field, swept by electromagnet, and $B_{0,\mathrm{res}}$ is the value of the magnetic field at which the resonance is observed. The spectrum recorded in the commercial electromagnet was simulated using the *pepper* function in the EasySpin library for MATLAB (Mathworks) [36]. From a least-squares analysis using *esfit* in EasySpin, $g = 2.0064$ and a linewidth of 0.25 mT (FWHM) were obtained after a phase correction of -0.08π (≈ -0.25 rad or $-14.4°$). The spectrum was then recorded in the portable electromagnet with a much smaller number of points, broadening the linewidth on the order of the size of the field steps when sweeping the field. To permit simulation of the recorded spectrum, the data were interpolated using a *modified Akima piecewise cubic Hermite interpolation* algorithm [40, 41] in MATLAB (Mathworks), resulting in an EPR spectrum with SNR = 105. The interpolated data were similarly simulated and fit by least-squares analysis to obtain $g = 1.9653$ and a line width of 0.73 mT after a phase correction of $+0.08\pi$ ($\approx +0.25$ rad or $+14.4°$).

4 Discussion

4.1 Estimation of EPR Capabilities During XAS Experiments

The portable EPRoC spectrometer was developed for EPR detection of radiation damage of samples during X-ray absorption spectroscopy experiments as well as for possible applications in measuring the accumulated irradiation dose in organic radicals such as in alanine, which is commonly used for industrial and medical dosimetry applications [8–12]. X-ray spectroscopic methods are commonly used for research in important organic and biologically active molecules, such as amino acids, nucleotides, and proteins. Typical XAS measurements are performed with X-rays with energies slightly above the binding energy of the electron shells of the atoms within the sample investigated. The increase in the X-ray absorption that occurs at this energy is referred to as the absorption edge. For instance, typical experiments for organic compounds are performed at the carbon K-edge (~ 284 eV), the oxygen K-edge (~ 532 eV), the nitrogen K-edge (~ 402 eV), and the phosphorus K-edge (~ 2146 eV) [42]. To estimate the feasibility of detecting paramagnetic species induced by X-ray radiation during XAS experiments using the portable EPRoC spectrometer, it was necessary to estimate the generation rate of alanine radicals (spins) when subjected to ionizing radiation.

The energy absorbed by the sample per second when irradiated by incident X-rays with energy E_{incident} [43, 44] can be written as follows,

$$E_{\text{absorbed}} = \Phi \cdot E_{\text{incident}}(1 - e^{-(\mu/\rho)\cdot x})$$

where Φ – photon flux, μ/ρ is the mass attenuation coefficient and $x = t \cdot \rho$, with t and ρ being the thickness and mass density of the sample accordingly, μ is the attenuation coefficient.

The typical photon flux for a synchrotron facility is 10^{12}–10^{13} photons per second [38]. The X-ray energies (E_{incident}) would then result in absorbed energy rates of ~ 45 μJ/s, 64 μJ/s, and 85 μJ/s for carbon, nitrogen and oxygen K-edges, respectively, and photon flux of 10^{12} photons/s.

The mass attenuation coefficient μ/ρ for alanine at a moderate energy of incident photons (~ 1000 eV) is 3064 cm^2/g [45]. Considering the sensitive area of the EPRoC, the absorbed energies within the alanine may be estimated from the total X-ray exposure time, the estimated thickness (120 μm) calculated based on the coil size and prior measurements of B_1 distributions in similar VCO coils, and the mass density (1.42 g/cm^3) of the material such that the absorbed energy rate corresponds to each atom considered (C, N, O).

To calculate the rate of absorbed radiation dose, the mass of the sample must be considered. The size of the incident beam varies for different XAS spectrometers but may in general be estimated as a circle with a diameter of 200 μm for synchrotron facilities [38, 44]. The beam size is greater than the sensitive area of the EPRoC such that the volume of an irradiated sample when measured by the portable EPR spectrometer can be estimated as 7.2 nL and is limited by the coil diameter of the EPRoC, resulting in a mass of ~ 10 μg of alanine irradiated within the coil. The rates of absorbed radiation dose are 4.5 kGy/s for the carbon K-edge, 6.4 kGy/s for the nitrogen K-edge and 8.5 kGy/s for the oxygen K-edge.

The dependence of the EPR signal amplitude of alanine on the radiation dose absorbed is approximately linear for doses up to ~ 100 kGy; however, for doses between 100 and 5000 kGy, the signal intensity initially ceases to increase before decreasing substantially at higher doses [8, 46, 47]. The calculated dose rates may then be used to estimate the rate at which the EPRoC signal will increase or decrease during XAS measurements. The EPRoC spectrum of alanine which yielded an SNR of 21.3 (Fig. 6) was recorded for a sample that was irradiated by gamma-radiation from a cobalt source with a total dose of 16 kGy and required 18 h of continuous measurement. It has been demonstrated that the relative response of alanine to X-ray radiation in the keV range in comparison with ^{60}Co radiation differs by approximately a factor of 0.6 [55]. Since the energies required for the XAS measurements of alanine are in the 0.3–2 keV range, the number of alanine radicals generated by gamma-radiation is used as an estimation for the number of the radicals generated by X-ray radiation. Considering the rates of absorption calculated above for the carbon, nitrogen, and oxygen K-edges of alanine during irradiation, the number of total spins required to achieve SNR of 3 with the EPRoC would be generated on the order of ~ 0.5–5 min while the typical measurement time for XAS experiments is on the order of 20 min. Therefore, the sweep time of the portable electromagnet is the limiting factor with respect to time during data acquisition. In the case of transition metal XAS measurements, Cu^{2+} ions, which are present in many catalysts [48–50] as well as some biologically active species

such as metalloproteins [51, 52] can be reduced during radiation damage to EPR-silent Cu^{+} states [44]. It has been demonstrated that surface grafted Cu(II)-tetramethylethylenediamine (Cu-TMEDA) species were rapidly degraded to Cu(I) upon irradiation using focused X-rays from a high brilliance source (10^{12}–10^{14} photons·mm^{-2}·s^{-1}). It was shown that fraction of Cu(I) states, observed in the XAS spectrum of the sample, increased from ~ 0.4 to ~ 0.8 after ten minutes of exposure to X-rays [22]. In some catalyst materials, the Cu(II) content can be quite high, such as in CuO-CeO_2 (up to 40% wt Cu) [53]. Given the mass density of the material (6.83 g/cm^3), the number of spins within the sensitive volume of the EPRoC was determined ($1.5 \cdot 10^{17}$ spins). The EPRoC measurements of the irradiated alanine sample demonstrated the spin sensitivity of $5.8 \cdot 10^{12}$ spins, which means that $5.8 \cdot 10^{12}$ spins can be recorded using the EPRoC in one hour with SNR = 3. Assuming the degradation rate of Cu(II) species during X-ray exposure is similar to the evolution rate of Cu(I) reported in Ref. [22] for Cu-TMEDA, after consideration of the differences in linewidths observed between Cu(II) and alanine, the resulting SNR after one minute of data collection would decrease from ~ 1000 to ~ 200 as the total number of spins decreases from 1.5 to $0.3 \cdot 10.^{17}$ spins. The environment under which EPR measurements are performed, such as temperature and chosen atmosphere, can affect the linewidth and amplitude of the signal, resulting in the change of SNR. In the examples included herein, normal atmosphere was used; however, in many cases removal of oxygen decreases the linewidth and increases signal intensity thereby improving SNR and it is under such an oxygen-free environment that EPR measurements would take place in the XAS chamber. Because the degradation occurs over just ten minutes of X-ray exposure, the resolution of the generation rate greatly depends on the sweep capabilities of the spectrometer, as was the case in the radical generation in alanine. However, improvement may be accomplished in several ways, such as by implementing modulation coils for rapid scan, performing frequency-swept acquisition at a single field, or by recording at a single field value after characterization of the generated radical [26, 28, 31, 33, 54].

4.2 Possible Improvements to the EPRoC-Based Spectrometer

During the initial evaluation of the spectrometer capabilities, a commercial electromagnet was first used to establish the performance of the EPRoC sensor independently of the portable electromagnet. In the recorded spectra, an intense baseline was observed that could be corrected using a polynomial function; however, the baseline varied between experiments. Additionally, spikes from the direct current were found to greatly inhibit the detection of samples with low spin concentration (Fig. S2). Relative to other EPRoC designs, an increased sensitivity to electrostatic discharge was observed. This likely contributes to the susceptibility of the EPRoC to environmental disturbances, especially those that might propagate through current and voltage supply systems or even within the grounding of the laboratory.

When the EPRoC was subsequently investigated together with the portable electromagnet, an EPR signal with an SNR = 105, after interpolation, was recorded using Li_2Pc placed directly on the coil. The linewidth was broadened by 0.5 (0.48)

mT relative to that observed in the commercial electromagnet and may partially be explained by the observed shift in the resonance position in the magnetic field by 6.6 mT likely caused by misalignment of the EPRoC within the portable electromagnet (see Supporting Information). Development of a sample holder for precise positioning of the EPRoC inside the most homogeneous region of the portable electromagnet would circumvent this; and, would likely be an additional requirement for installation of the spectrometer into a synchrotron beamline. Acquiring Hall probes with smaller field resolution would provide the possibility to measure samples with smaller linewidths, considering the resolution of the Hall probes used (0.1 mT) were on the order of the linewidth observed in the commercial electromagnet (0.25 mT). The initial design of the portable EPRoC spectrometer did not require sweeping of the magnetic field, rather only coarse adjustment would be utilized to position the resonance field within the bandwidth of the EPRoC device (6.656–7.056 GHz) which could be swept and recorded as the frequency-swept, frequency-modulated EPR signal. However, it was determined that operating at a single microwave frequency, which employs a constant voltage rather than a swept voltage, reduced the likelihood of failure due to electrostatic discharge. Therefore, field-sweep capabilities of the portable electromagnet were investigated. It was anticipated that the resolution of the Hall probes was sufficient to allow the acquisition of EPR spectra of alanine and Cu(II) containing materials using the EPRoC and portable electromagnet.

5 Conclusions

The current work outlines the capabilities of an EPRoC-based spectrometer, designed for integration into an X-ray absorption spectrometer to simultaneously detect radiation damage in materials via EPR while performing XAS experiments. The design of the spectrometer consists of BiCMOS EPRoC sensor and portable electromagnet, which were evaluated first separately for their capabilities before being assessed as a complete spectrometer. A linear dependence on spin concentration was found when using the EPRoC sensor to record the EPR spectra of varying concentrations of tempol in sucrose octaacetate. The sensitivity of the EPRoC sensor was found to be on the order of 10^{13} spins per hour when recording the EPR spectra of alanine, which is sufficient for detection of the X-ray induced generation of alanine radicals and reduction of Cu(II) according to estimations of total spins present in the EPRoC after considerations of linewidth. When performing measurements of Li_2Pc using both the EPRoC sensor and the portable electromagnet, the minimum spin concentration and linewidth detectable was found to be $0.24 \cdot 10^{19}$ spins/ml and 1mT, respectively (see Supporting Information).

To record EPR spectra on a relevant timescale, the measurements must be performed in less than one minute. This will be accomplished by incorporating faster sweep methods into the spectrometer design, such as the inclusion of small and more agile sweep coils for rapid scan measurements [33, 54, 56] or by revisiting frequency-sweep capabilities. The EPRoC sensor can be further

modified via fabrication of a hole in the VCO coil using FIB to allow X-rays to pass through the EPRoC sensor. While successful hole drilling was demonstrated, the corresponding ERRoC was not used within the current work. Similar hole fabrication in other EPRoC sensors has demonstrated that FIB milling does not create any detectable defects when using EPRoC sensors and allows for an increase in sensitivity by increasing the total accessible sensitive volume of the VCO coil [37]. These improvements will dramatically increase the potential success towards implementation of an EPRoC spectrometer in a synchrotron beamline for measurement during XAS experiments.

Supplementary Information The online version contains supplementary material available at https://doi.org/10.1007/s00723-024-01702-7.

Acknowledgements We acknowledge Elizaveta Kobeleva from Department of Physics of Freie Universität Berlin for her calculations of the dose, which was used to irradiate the sample. We thank Markus Bär and his group from Department Interface Design at Helmholtz-Zentrum Berlin (HZB) for sharing their expertise on X-ray Absorption Spectroscopy. We are very thankful to Silvio Künstner, Michele Segantini and Boris Naydenov from Department Spins in Energy Conversion and Quantum Information Science of HZB as well as Alexander Schnegg from Max-Plank-Institute for Chemical Energy Conversion and EPRoC consortium for their fruitful discussions.

Author Contributions KL, JM and ES defined the goals of research. JM and ES designed the experiments. HL, AS, MH, MK and JA designed the EPRoC. AS and MH designed the printed circuit board (PCB) for the EPRoC. HL, AS, MH and MK performed electrical characterization of the EPRoC and PCB. MN, RG, BK and KK designed and fabricated the portable electromagnet. ES and BK tested the portable electromagnet. ES and GM developed a python-based script for control of the portable electromagnet. ES and AT tested the fabrication of the hole inside the EPRoC. KH provided access, training, and support with the FIB technique. AD and AD performed the irradiation of the alanine samples. ES and JM performed the EPRoC measurements and data processing. ES, JM and KL evaluated the experimental results. ES and JM wrote the manuscript. All authors revised the manuscript and agreed to the published version.

Funding Open Access funding enabled and organized by Projekt DEAL. This research has been supported by the Bundesministerium für Bildung und Forschung under contract number 01186916/1 (EPRoC), by the HEMF (Helmholtz Energy Materials Foundry) infrastructure funded by the Helmholtz association (HGF), and by the DFG priority program INtegrated TERahErtz sySTems Enabling Novel Functionality (INTEREST) (SPP 2314). This research was carried out within the Helmholtz International Re- search School (HIRS-0008), "Hybrid Integrated Systems for Conversion of Solar Energy" (HI-SCORE), an initiative co-funded by the "Initiative and Networking Fund of the Helmholtz Association".

Data Availability No datasets were generated or analysed during the current study.

Declarations

Conflict of Interest The authors declare no competing interests.

References

1. M.F. Desrosiers, G.L. Wilson, C.R. Hunter, D.R. Hutton, Estimation of the absorbed dose in radiation-processed food—1. Test of the EPR response function by a linear regression analysis. Int. J. Radiat. Appl. Instrum. Part A Appl. Radiat. Isotopes **42**(7), 613–616 (1991). https://doi.org/10.1016/0883-2889(91)90030-5
2. J. Raffi, S. Gelly, L. Barral, F. Burger, P. Piccerelle, P. Prinderre, M. Baron, A. Chamayou, Electron paramagnetic resonance of radicals induced in drugs and excipients by radiation or mechanical treatments. Spectrochim. Acta Part A Mol. Biomol. Spectrosc. **58**(6), 1313–1320 (2002). https://doi.org/10.1016/S1386-1425(01)00720-X
3. M. Gibella, A.-S. Crucq, B. Tilquin, P. Stocker, G. Lesgards, J. Raffi, Electron spin resonance studies of some irradiated pharmaceuticals. Radiat. Phys. Chem. **58**(1), 69–76 (2000). https://doi.org/10.1016/S0969-806X(99)00353-9
4. A. Chiappinelli, M. Mangiacotti, M. Tomaiuolo, G. Trotta, G. Marchesani, A.E. Chiaravalle, Identification of X-ray-irradiated hazelnuts by electron spin resonance (ESR) spectroscopy. Eur. Food Res. Technol. **245**(10), 2323–2329 (2019). https://doi.org/10.1007/s00217-019-03349-2
5. K.I. Aleksieva, N.D. Yordanov, Various approaches in EPR identification of gamma-irradiated plant foodstuffs: a review. Food Res. Int. **105**, 1019–1028 (2018). https://doi.org/10.1016/j.foodres.2017.11.072
6. S. Wilczyński, B. Pilawa, R. Koprowski, Z. Wróbel, M. Ptaszkiewicz, J. Swakoń, P. Olko, Free radicals properties of gamma-irradiated penicillin-derived antibiotics: piperacillin, ampicillin, and crystalline penicillin. Radiat. Environ. Biophys. **53**(1), 203–210 (2014). https://doi.org/10.1007/s00411-013-0498-1
7. U. Hochkirch, W. Herrmann, R. Stößer, K.-P. Moll, J. Gallego Llerena, M. Linscheid, H.-H. Borchert, Determination of spin concentrations in ESR tomography as applied for the spatial distribution of spin labels in human skin. Appl. Magn. Reson. **35**(1), 173–184 (2008). https://doi.org/10.1007/s00723-008-0142-4
8. M.F. Desrosiers, J.M. Puhl, S.L. Cooper, An absorbed-dose/dose-rate dependence for the alanine-EPR dosimetry system and its implications in high-dose ionizing radiation metrology. J. Res. Nat. Inst. Stand. Technol. **113**(2), 79 (2008). https://doi.org/10.6028/jres.113.007
9. U. Gohs, Application of an alanine dosimetry system for industrial irradiation and radiation protection. Appl. Radiat. Isot. **47**(11–12), 1169–1170 (1996). https://doi.org/10.1016/S0969-8043(96)00133-9
10. K. Mehta, R. Girzikowsky, Alanine-ESR dosimetry for radiotherapy IAEA experience. Appl. Radiat. Isot. **47**(11–12), 1189–1191 (1996). https://doi.org/10.1016/S0969-8043(96)00164-9
11. K. Gall, M. Desrosiers, D. Bensen, C. Serago, Alanine EPR dosimeter response in proton therapy beams. Appl. Radiat. Isot. **47**(11–12), 1197–1199 (1996). https://doi.org/10.1016/S0969-8043(96)00201-1
12. O. Baffa, A. Kinoshita, Clinical applications of alanine/electron spin resonance dosimetry. Radiat. Environ. Biophys. **53**(2), 233–240 (2014). https://doi.org/10.1007/s00411-013-0509-2
13. A.B. Flood, B.B. Williams, W. Schreiber, G. Du, V.A. Wood, M.M. Kmiec, S.V. Petryakov, E. Demidenko, H.M. Swartz, Advances in in vivo EPR tooth biodosimetry: meeting the targets for initial triage following a large-scale radiation event. Radiat. Prot. Dosimetry **172**(1–3), 72–80 (2016). https://doi.org/10.1093/rpd/ncw165
14. C.-C. Lu, H.-H. Lin, C.-H. Hsu, F.-N. Wang, J.-P. Lin, L.-H. Lai, Potential use of environmental biological samples for retrospective electron paramagnetic resonance dosimetry of radiation accidents. Appl. Sci. **10**(19), 6867 (2020). https://doi.org/10.3390/app10196867
15. E.I. Solomon, R.G. Hadt, Recent advances in understanding blue copper proteins. Coord. Chem. Rev. **255**(7–8), 774–789 (2011). https://doi.org/10.1016/j.ccr.2010.12.008
16. J.K. Kowalska, A.W. Hahn, A. Albers, C.E. Schiewer, R. Bjornsson, F.A. Lima, F. Meyer, S. DeBeer, X-ray absorption and emission spectroscopic studies of $[L_2Fe_2S_2]^n$ model complexes: implications for the experimental evaluation of redox states in iron–sulfur clusters. Inorg. Chem. **55**(9), 4485–4497 (2016). https://doi.org/10.1021/acs.inorgchem.6b00295
17. W.R. Hagen, EPR spectroscopy of complex biological iron–sulfur systems. J. Biol. Inorg. Chem. **23**(4), 623–634 (2018). https://doi.org/10.1007/s00775-018-1543-y

18. C. Gervais, M. Thoury, S. Réguer, P. Gueriau, J. Mass, Radiation damages during synchrotron X-ray micro-analyses of Prussian blue and zinc white historic paintings: detection, mitigation and integration. Appl. Phys. A **121**(3), 949–955 (2015). https://doi.org/10.1007/s00339-015-9462-z
19. M. Kubin, J. Kern, M. Guo, E. Källman, R. Mitzner, V.K. Yachandra, M. Lundberg, J. Yano, P. Wernet, X-ray-induced sample damage at the Mn L-edge: a case study for soft X-ray spectroscopy of transition metal complexes in solution. Phys. Chem. Chem. Phys. **20**(24), 16817–16827 (2018). https://doi.org/10.1039/C8CP03094D
20. A. Zabilska, A.H. Clark, D. Ferri, M. Nachtegaal, O. Kröcher, O.V. Safonova, Beware of beam damage under reaction conditions: X-ray induced photochemical reduction of supported VO_x catalysts during in situ XAS experiments. Phys. Chem. Chem. Phys. **24**(36), 21916–21926 (2022). https://doi.org/10.1039/D2CP02721F
21. R.S.K. Ekanayake, V.A. Streltsov, S.P. Best, C.T. Chantler, Using XAS to monitor radiation damage in real time and post-analysis, and investigation of systematic errors of fluorescence XAS for Cu-bound amyloid-β. J. Appl. Crystallogr. **57**(1), 125–139 (2024). https://doi.org/10.1107/S1600576723010890
22. M.A. Newton, A.J. Knorpp, J. Meyet, D. Stoian, M. Nachtegaal, A.H. Clark, O.V. Safonova, H. Emerich, W. van Beek, V.L. Sushkevich, J.A. van Bokhoven, Unwanted effects of X-rays in surface grafted copper(II) organometallics and copper exchanged zeolites, how they manifest, and what can be done about them. Phys. Chem. Chem. Phys. **22**(13), 6826–6837 (2020). https://doi.org/10.1039/D0CP00402B
23. A. Yokoya, K. Akamatsu, EPR spectrometer installed in a soft X-ray beamline at SPring-8 for biophysical studies. Nucl. Instrum. Methods Phys. Res. Sect. A **467–468**, 1333–1337 (2001). https://doi.org/10.1016/S0168-9002(01)00661-1
24. S. Calvin, *XAFS for Everyone* (CRC Press, 2013). https://doi.org/10.1201/b14843
25. M. Wang, L. Árnadóttir, Z.J. Xu, Z. Feng, In situ X-ray absorption spectroscopy studies of nanoscale electrocatalysts. Nano-Micro Lett. **11**(1), 47 (2019). https://doi.org/10.1007/s40820-019-0277-x
26. J. Anders, K. Lips, MR to go. J. Magn. Reson. **306**, 118–123 (2019). https://doi.org/10.1016/j.jmr.2019.07.007
27. M. Segantini, G. Marcozzi, D. Djekic, A. Chu, D. Amkreutz, C.T. Trinh, S. Neubert, B. Stannowski, K. Jacob, I. Rudolph, J.E. McPeak, J. Anders, B. Naydenov, K. Lips, Electrically detected magnetic resonance on a chip (EDMRoC) for analysis of thin-film silicon photovoltaics. Magnetochemistry **9**(7), 183 (2023). https://doi.org/10.3390/magnetochemistry9070183
28. M. Segantini, G. Marcozzi, T. Elrifai, E. Shabratova, K. Höflich, M. Daeconeasa, V. Niemann, R. Pietig, J. E. McPeak, J. Anders, B. Naydenov, & K. Lips, Compact electron paramagnetic resonance on a chip spectrometer using a single sided permanent magnet. ACS Sensors. *Under Review at the time of submission* (2024)
29. S. Künstner, J. E. McPeak, A. Chu, M. Kern, M. Wick, K. P. Dinse, J. Anders, B. Naydenov, & K. Lips, Microwave field mapping for EPR on a chip experiments. Sci. Adv. **10**, eado5467 (2024). https://doi.org/10.1126/sciadv.ado5467
30. J.M. Binder, A. Stark, N. Tomek, J. Scheuer, F. Frank, K.D. Jahnke, C. Müller, S. Schmitt, M.H. Metsch, T. Unden, T. Gehring, A. Huck, U.L. Andersen, L.J. Rogers, F. Jelezko, Qudi: a modular python suite for experiment control and data processing. SoftwareX **6**, 85–90 (2017). https://doi.org/10.1016/j.softx.2017.02.001
31. J. Handwerker, B. Schlecker, U. Wachter, P. Radermacher, M. Ortmanns, & J. Anders, 28.2 A 14GHz battery-operated point-of-care ESR spectrometer based on a 0.13µm CMOS ASIC. 2016 IEEE International Solid-State Circuits Conference (ISSCC), 476–477 (2016). https://doi.org/10.1109/ISSCC.2016.7418114
32. A. Chu, B. Schlecker, J. Handwerker, S. Kunstner, M. Ortmanns, K. Lips, J. Anders, VCO-based ESR-on-a-chip as a tool for low-cost, high-sensitivity food quality control. IEEE Biomed. Circ. Syst. Conf. (BioCAS) **2017**, 1–4 (2017). https://doi.org/10.1109/BIOCAS.2017.8325172
33. S. Künstner, A. Chu, K.-P. Dinse, A. Schnegg, J.E. McPeak, B. Naydenov, J. Anders, K. Lips, Rapid-scan electron paramagnetic resonance using an EPR-on-a-chip sensor. Magn. Reson. **2**(2), 673–687 (2021). https://doi.org/10.5194/mr-2-673-2021
34. T. Yalcin, G. Boero, Single-chip detector for electron spin resonance spectroscopy. Rev. Sci. Instrum. (2008). https://doi.org/10.1063/1.2969657
35. J. Anders, A. Angerhofer, G. Boero, K-band single-chip electron spin resonance detector. J. Magn. Reson. **217**, 19–26 (2012). https://doi.org/10.1016/j.jmr.2012.02.003

36. S. Stoll, A. Schweiger, EasySpin, a comprehensive software package for spectral simulation and analysis in EPR. J. Magn. Reson. **178**(1), 42–55 (2006). https://doi.org/10.1016/j.jmr.2005.08.013
37. M.A. Hassan, M. Kern, A. Chu, G. Kalra, E. Shabratova, A. Tsarapkin, N. MacKinnon, K. Lips, C. Teutloff, R. Bittl, J.G. Korvink, J. Anders, Towards single-cell pulsed EPR using VCO-based EPR-on-a-chip detectors. Frequenz **76**(11–12), 699–717 (2022). https://doi.org/10.1515/freq-2022-0096
38. K. Sigfridsson Clauss, K. Klementiev, J. Just, S. Nehzati, M. Ramakrishnan, D. Haase, S. Carlson, & S. Ansell, Balder beamline MAX IV beamline review report. MAX IV Laboratory, Lund University, Lund. (2023). Available: https://www.maxiv.lu.se/beamlines-accelerators/beamlines/balder/ [2024, March 13]
39. J.W. Ward, R.L. Kubena, M.W. Utlaut, Transverse thermal velocity broadening of focused beams from liquid metal ion sources. J. Vacuum Sci. Technol. B **6**, 2090 (1988). https://doi.org/10.1116/1.584117
40. H. Akima, A new method of interpolation and smooth curve fitting based on local procedures. J. ACM **17**(4), 589–602 (1970). https://doi.org/10.1145/321607.321609
41. H. Akima, A method of bivariate interpolation and smooth surface fitting based on local procedures. Commun. ACM **17**(1), 18–20 (1974). https://doi.org/10.1145/360767.360779
42. J.A. Bearden, A.F. Burr, Reevaluation of X-ray atomic energy levels. Rev. Mod. Phys. **39**(1), 125–142 (1967). https://doi.org/10.1103/RevModPhys.39.125
43. O.B. Zeldin, M. Gerstel, E.F. Garman, RADDOSE-3D: time- and space-resolved modelling of dose in macromolecular crystallography. J. Appl. Crystallogr. **46**(4), 1225–1230 (2013). https://doi.org/10.1107/S0021889813011461
44. U. Molich, Improving methods for X-ray absorption spectroscopy studies of metalloproteins. Technical University of Denmark (2020)
45. J.H. Hubbell & S.M. Seltzer, Tables of X-ray mass attenuation coefficients and mass energy-absorption coefficients (version 1.4). National Institute of Standards and Technology, Gaithersburg, MD. (2004). Available: https://doi.org/10.18434/T4D01F [2024, March 13]
46. B. Ciesielski, L. Wielopolski, The effects of dose and radiation quality on the shape and power saturation of the EPR signal in alanine. Radiat. Res. **140**(1), 105 (1994). https://doi.org/10.2307/3578575
47. B. Ciesielski, Combined effects of high doses and temperature on radiation-induced radicals and their relative contributions to EPR signal in gamma-irradiated alanine. Radiat. Prot. Dosimetry **120**(1–4), 184–190 (2006). https://doi.org/10.1093/rpd/nci503
48. G.S. More, A. Shivhare, S.P. Kaur, T.J. Dhilip Kumar, R. Srivastava, Catalytic interplay of metal ions (Cu^{2+}, Ni^{2+}, and Fe^{2+}) in MFe_2O_4 inverse spinel catalysts for enhancing the activity and selectivity during selective transfer hydrogenation of furfural into 2-methylfuran. Catal. Sci. Technol. **12**(15), 4857–4870 (2022). https://doi.org/10.1039/D2CY00970F
49. U. Iacobone, I. Nova, E. Tronconi, R. Villamaina, M.P. Ruggeri, J. Collier, D. Thompsett, Appraising multinuclear Cu^{2+} structure formation in Cu-CHA SCR catalysts via low-T dry CO oxidation with modulated NH_3 solvation. ChemistryOpen (2022). https://doi.org/10.1002/open.202200186
50. X. Zhou, J. Shan, L. Chen, B.Y. Xia, T. Ling, J. Duan, Y. Jiao, Y. Zheng, S.-Z. Qiao, Stabilizing Cu^{2+} ions by solid solutions to promote CO_2 electroreduction to methane. J. Am. Chem. Soc. **144**(5), 2079–2084 (2022). https://doi.org/10.1021/jacs.1c12212
51. L. Rulíšek, J. Vondrášek, Coordination geometries of selected transition metal ions (Co^{2+}, Ni^{2+}, Cu^{2+}, Zn^{2+}, Cd^{2+}, and Hg^{2+}) in metalloproteins. J. Inorg. Biochem. **71**(3–4), 115–127 (1998). https://doi.org/10.1016/S0162-0134(98)10042-9
52. G.C. Schröder, F. Meilleur, Metalloprotein catalysis: structural and mechanistic insights into oxidoreductases from neutron protein crystallography. Acta Crystallographica Sect. D Struct. Biol. **77**(10), 1251–1269 (2021). https://doi.org/10.1107/S2059798321009025
53. F. Wang, R. Büchel, A. Savitsky, M. Zalibera, D. Widmann, S.E. Pratsinis, W. Lubitz, F. Schüth, In situ EPR study of the redox properties of CuO–CeO_2 catalysts for preferential CO Oxidation (PROX). ACS Catal. **6**(6), 3520–3530 (2016). https://doi.org/10.1021/acscatal.6b00589
54. J. Möser, K. Lips, M. Tseytlin, G.R. Eaton, S.S. Eaton, A. Schnegg, Using rapid-scan EPR to improve the detection limit of quantitative EPR by more than one order of magnitude. J. Magn. Reson. **281**, 17–25 (2017). https://doi.org/10.1016/j.jmr.2017.04.003
55. P. van den Elzen, T. Sander, H. Palmans, M. McManus, N. Woodall, N. Lee, O.J.L. Fox, R.M. Jones, D. Angal-Kalinin, A. Subiel, Alanine response to low energy synchrotron x-ray radiation. Phys. Med. Biol. **68**(6), 065011 (2023). https://doi.org/10.1088/1361-6560/acb886

56. G. R. Eaton & S. S. Eaton, Rapid-scan electron paramagnetic resonance. In eMagRes (pp. 1529–1542). John Wiley & Sons, Ltd (2016). https://doi.org/10.1002/9780470034590.emrstm1522

Authors and Affiliations

Ekaterina Shabratova[1,5] · Hadi Lotfi[2] · Ayman Sakr[2] · Mohamed Atef Hassan[2] · Michal Kern[2] · Matthias Neeb[4] · René Grüneberger[4] · Bastian Klemke[4] · Gianluca Marcozzi[1,3] · Klaus Kiefer[4] · Aleksei Tsarapkin[5] · Katja Höflich[5] · Alina Dittwald[6] · Andrea Denker[6] · Jens Anders[2] · Joseph E. McPeak[1,7] · Klaus Lips[1,3]

✉ Joseph E. McPeak
joseph.mcpeak@helmholtz-berlin.de

1 Berlin Joint EPR Laboratory and EPR4Energy, Department of Spins in Energy Conversion and Quantum Information Science (ASPIN), Helmholtz-Zentrum Berlin für Materialien und Energie GmbH (HZB), Berlin, Germany

2 Institut für Intelligente Sensorik und Theoretische Elektrotechnik, Universität Stuttgart, Stuttgart, Germany

3 Berlin Joint EPR Laboratory, Fachbereich Physik, Freie Universität Berlin, Berlin, Germany

4 Department Sample Environment, Helmholtz-Zentrum Berlin für Materialien und Energie GmbH (HZB), Berlin, Germany

5 Ferdinand-Braun-Institut, Leibniz-Institut für Höchstfrequenztechnik (FBH), Berlin, Germany

6 Department Protons for Therapy, Helmholtz-Zentrum Berlin für Materialien und Energie GmbH (HZB), Berlin, Germany

7 Department of Chemistry, Novo Nordisk Foundation Pulse EPR Center, University of Copenhagen, Copenhagen, Denmark